

UNSTRUCTURED MESH CAPABILITES FOR SUPERSONIC WING DESIGN AT LOW SPEED CONDITIONS

Michele Gaffuri*, Joël Brezillon*

*German Aerospace Center, Institute of Aerodynamics and Flow Technology
Lilienthalplatz 7, D-38108 Braunschweig
e-mail: {michele.gaffuri,joel.brezillon}@dlr.de

Key words: CFD, MDO, Vortex dominated flow, Unstructured mesh, Supersonic wing, High lift devices

Abstract. *In this paper the reliability of using unstructured meshes for the CFD simulation of the flow over a low aspect-ratio wing in low speed configuration is investigated. It is intended to integrate such mesh strategy in a high-fidelity aerodynamic shape optimization loop for the design of high lift devices, so particular care is given to the set-up of a suitable meshing procedure usable in optimization context. Meshes are created using the grid generators Solar and Centaur; the CFD analysis is carried out using the DLR-TAU solver on the EPISTLE wing-body configuration with drop-nose slat. Results are compared to wind tunnel test data and to CFD results obtained on a structured mesh. It is shown that a grid of around 10 million points, if carefully conceived, is able to predict with reasonably good accuracy the aerodynamic loads and the overall flow features. Some discrepancies in the detection of vortical flow features are found, but they do not have significant influence on the computed loads. The application of the method at various Reynolds numbers confirms the importance of the prismatic layer thickness to accurately capture the vortical flow features.*

1 INTRODUCTION

Three dimensional, high fidelity shape optimization of an aircraft at take-off and landing conditions sets some challenges to the engineer, especially when designing a supersonic aircraft. In the case of highly swept, thin, low aspect ratio wings the flow is vortex dominated and thus highly complex. Computational fluid dynamics (CFD) analysis on this type of configuration can be carried out using structured hexahedral grids [1] [2] or unstructured hybrid grids, composed with a mix of hexahedral, prismatic and tetrahedral cells. Building a structured, multiblock, hexahedral mesh for a complex geometry that includes high lift devices (HLD), control surfaces and nacelles is an extremely time consuming task. Contrarily, unstructured meshes could provide the necessary flexibility to represent complex and changing geometries in a reliable and fast way. With this approach however, the problem of computational cost arises since for achieving the same accuracy as with structured meshes the number of grid points has to be increased: in the context of finite volume CFD solvers, the aspect ratio of the tetrahedral cells has to be kept small in order to ensure a good flow resolution while hexahedra with large aspect ratio can be advantageously used to discretise the wing surface.

Keeping a reasonable computational cost is also an issue when dealing with vortical flows, where the vortices may rapidly diffuse when using too coarse tetrahedral meshes. The use of grid adaptation [3] allows the increase of the flow accuracy by refining the mesh only where the flow resolution has to be increased. When doing HLD design however grid adaptation is often problematic for two reasons: firstly the turnaround time for a CFD computation may be too high for the design phase, when typically one wants to analyze many different configurations; secondly when the design process is carried out using an aerodynamic shape optimization framework [4], the optimum may move towards better grid adaptation and not towards better aerodynamic performances.

In the present work a systematic study on unstructured meshes is performed in order to assess their qualities for the design of a delta wing featuring HLD.

Section 2 describes the tools employed in the project, the geometry used for the study and the available data. Section 3 gives a description of the mesh generation process. The resulting grids are assessed at several flow conditions in section 4. At the same time the influence of several turbulence models is assessed. These results are finally discussed in section 5.

2 TOOLS AND METHODS

2.1 Case study

The analysis is carried out on the EPISTLE [5] wing-body configuration. This supersonic delta wing concept has a blunt leading edge and includes, in its take-off and landing configuration, a long non slotted slat designed by the DLR during the EPISTLE European project. Experimental data are available on this configuration at various Reynolds numbers and angles of incidence.

A 4.2 million points structured mesh with a C-topology is also available (see left hand side of Figure 2). It has been originally built by NLR during the EPISTLE project and was proven to be fine enough to well capture the flow physics. The C-shape ensures that the region downstream of the wing trailing edge is correctly resolved. New CFD computations on this mesh are carried out and are considered as reference for the present analysis.

2.2 Mesh generation

The guidelines for mesh generation established during the EPISTLE project [6] are used as a first guess for the setup of the grid generation. Two unstructured mesh generators are considered: Centaur [7] and Solar [8]. Both are hybrid mesh generators: they create a near field prismatic mesh for the correct capture of the boundary layer and an outer tetrahedral mesh. Main difference between the two is that Centaur creates triangular surface meshes while Solar creates quad dominant surface meshes. Accuracy of the solution, mesh sizes and possibility of automatic mesh generation are used as terms of the comparison between the meshing tools used. The created meshes can be considered O-shaped, since the prismatic layer region completely surrounds the geometry. This is a drawback of the unstructured methodology: creating a C-shaped hybrid grid for a thick trailing edge wing, although possible, would have required extensive CAD manipulation: this would have been a problem in view of the integration in the optimization process.

2.3 CFD flow solver

Numerical simulations are carried out using the DLR-TAU unstructured finite volume solver [9]. The Reynolds-averaged Navier-Stokes equations are solved using a second order central space scheme with artificial matrix dissipation and an implicit Euler temporal scheme. The system is solved using the LUSGS method. Three models are used for the additional turbulence equations: the one equation Spalart-Allmaras model [10] with Edwards modification [11], Menter's 2 equations SST $k-\omega$ model [12] and a Reynolds Stress model based on the Speziale-Sarkar-Gatski model in the field and on the Launder-Reece-Rodi near the walls [13]. Turbulence modelling is especially important for this type of configurations since it can have an impact on the vortex onset location. On a smooth surface such as a blunt leading edge wing the vortex development strongly depends on the Reynolds number, thus correct estimation of viscous phenomena is capital to correctly estimate the suction effect of the vortex.

Computations are done on the DLR CASE cluster, a recently updated Linux cluster system consisting of 640 nodes. Each node is equipped with two 6-cores Intel Xeon processors and 24 GB of RAM memory. Most of the computations have been done before the update, when the nodes were equipped with two 4-cores Xeon. The DLR-TAU code runs in parallel on the cluster thanks to an MPI approach. Computations on the unstructured mesh are performed using 8 nodes, while on the structured mesh between 4

and 6 nodes were used, depending on the cluster load.

2.4 Wind tunnel data

The geometry was tested during 2 wind tunnel campaigns. A first campaign was conducted in the frame of the European project EPISTLE at the ONERA F1 wind tunnel facility in 2001 . The pressurised wind tunnel (max ambient pressure: 3.4 bar) allowed the testing with flow parameters similar to the flight conditions: Reynolds numbers up to 22.5 millions were reached, with a Mach number of 0.25. The 1:22 scaled steel model was mounted on a three struts device for this test campaign.

For assessing the accuracy of the CFD method at high Reynolds numbers, we use the CFD results on the aforementioned structured mesh, which are validated towards these WT data.

A second test campaign took place on the same model in 2003 at the DNW-NWB wind tunnel located in Braunschweig, Germany. This time the model was mounted on a rear sting support. Tests have been performed at 2 Reynolds numbers: 5 millions and 6.5 millions. In addition to forces and moments data, some oil flow pictures have been generated during the tests.

The model is equipped with about 500 pressure sensors. In the present work pressure data on four wing sections ($y_1 = 0.241$, $y_2 = 0.361$, $y_3 = 0.582$, $y_4 = 0.806$) are used in order to assess the CFD results.

2.5 Test case conditions

The reference case considered has a Mach number of 0.25, a Reynolds number of $22.5 \cdot 10^6$ and an angle of attack of 11.22° . This case is analyzed in detail, but CFD simulations are also carried out at other conditions - low Reynolds number computations ($Re=5 \cdot 10^6$, $Re=6.5 \cdot 10^6$) and complete polars at the aforementioned flight conditions - in order to be able to draw more general conclusions. CFD computations are always performed on the half geometry, taking advantage of the geometry and flow symmetry.

3 UNSTRUCTURED MESH GENERATION

The main idea behind the unstructured mesh generation strategy is the maximization of the prismatic layer thickness. In fact the accuracy of the prisms is higher than that of the tetrahedra, so in the ideal case, we would like to extend the prismatic layer so that the vortical flows completely reside in it.

Efforts are made to reduce as much as possible the total number of points used in the mesh. A value in the order of 10 million points is considered as the maximum practical mesh size for the successive design and optimization phases.

3.1 Solar mesh

Mesh generation in BAE Systems' software Solar (version 14 is used) is setup using the Java front-end Raven. The geometry has to be input in IGES format. Preparation steps include the aggregation of surfaces in zones, the definition of trimmed surfaces, the creation of the far-field surface and the symmetry plane, and the creation of so called sources: entities that define the required cell size, as well as the cells' anisotropy, at selected locations. In practice many sourcing strategies are built-in so one only has to choose a surface (e.g. the wing surface) and the corresponding sourcing method ("wing anisotropic fine", for example). Nevertheless, as these meshing strategies are developed for conventional (i.e. Airbus/Boeing like) transport aircrafts, the sources have to be modified in order to create a good quality mesh for the case at hand.

Surface mesh generation is based on an advancing front technique and creates mainly quadrilaterals. A structured surface mesh can be created on quadrilateral, untrimmed surfaces: it is advised to use this feature on the wing trailing edges. From the surface mesh the prismatic layer is grown with an advancing layer method, with parameters defined by the user to account for the required flow to be resolved. In this study the prismatic mesh is set as to have a y^+ of 1 according to flat plate theory. Finally the tetrahedral outer mesh is created using a constrained Delauney method and connected to the prismatic zone via a layer of pyramids.

The number of prismatic layers is not selected directly by the user. Instead, based on the defined first cell height and growth ratio, the number of layers to be generated is chosen so that the cell aspect ratio in the last layer is 1. This has the effect that refining the surface grid reduces the total height of the prismatic layer. A trade-off has to be found between spanwise and chordwise resolution on one hand, and prismatic layer height on the other.

Another critical point is the wing-fuselage intersection. It is known that hybrid grid generators have problems in creating the prismatic layer in presence of angles. The total height of the prismatic layer is reduced either by reducing the first cell height or by decreasing the total number of cells (a process called "chopping"). The end result is that the first tetrahedral cell at the intersection is too coarse to correctly resolve the flow. During the meshing process using Solar, no surface mesh refinement has been performed at the intersection, in an effort to keep the prismatic layer thickness as large as possible. The price to pay is the low resolution of the tetrahedral mesh near the intersection (Figure 1).

Before being able to use the mesh in a CFD simulation two additional steps are required. First, since Solar can create elements not accepted by the flow solver TAU (namely elements with hanging faces) the mesh has to be modified to eliminate them by splitting or collapsing cells. A tool (called `make_conform`) exists to perform this action. Secondly the mesh smoothness can be increased significantly using the DLR-TAU grid tools. This process takes a couple of minutes but can increase the convergence rate of the CFD computation significantly.

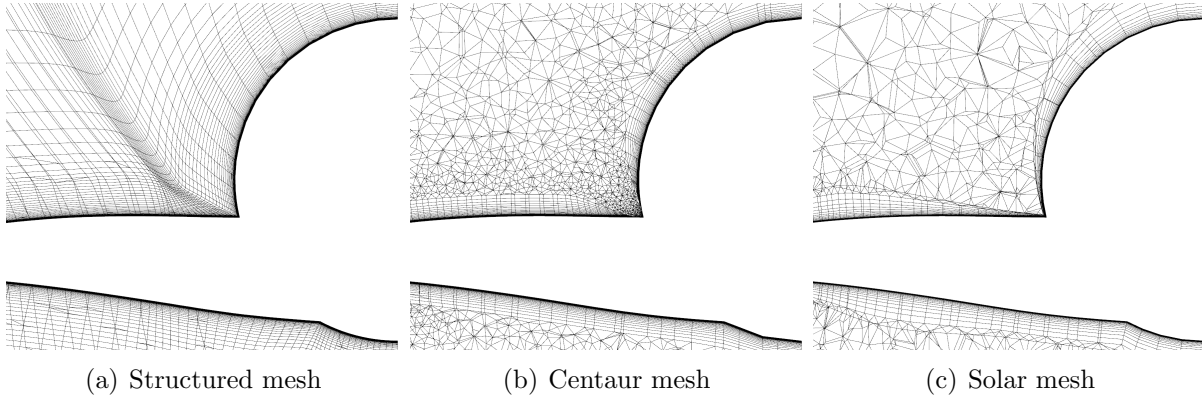


Figure 1: Mesh slices normal to the longitudinal (x) axis at location $x=2m$.

It has to be noted that Solar has sometimes trouble when connecting the far-field mesh to the prismatic layer (more precisely, to the buffer layer of pyramids and tetrahedra surrounding the prism layer). This is usually caused by the excessive anisotropy of the surface mesh. In this case decreasing the anisotropy value of the sources is required to get a valid volume mesh. The price to pay is an increase in the total number of grid points.

After several tests the final mesh used for the study consists of 11.5 million points with 33 layers of prismatic cells (Figure 2 right).

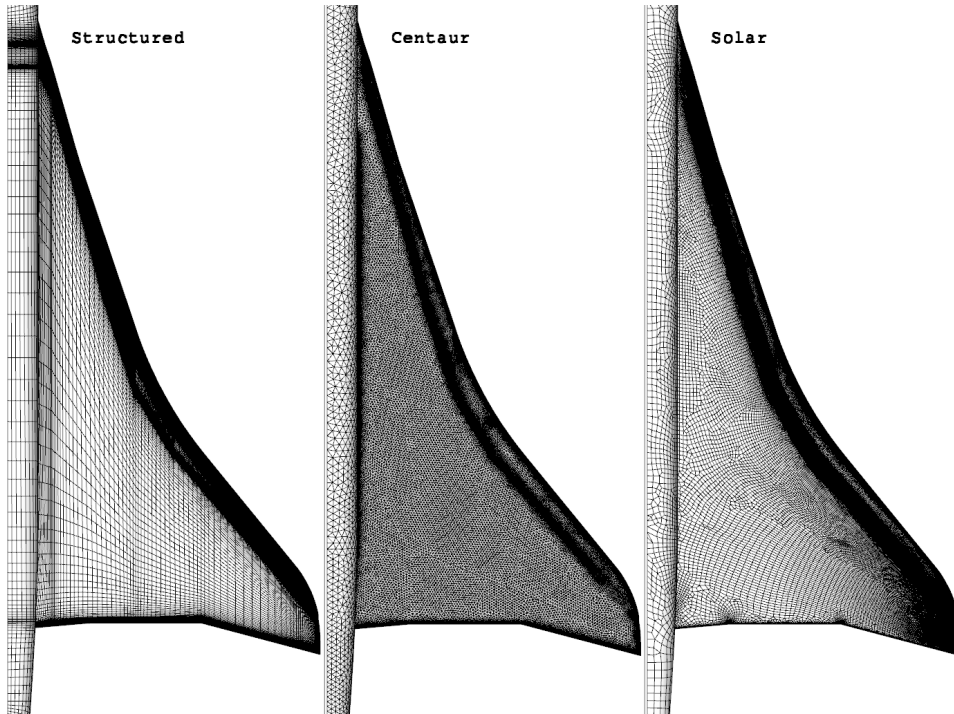


Figure 2: Fuselage and wing suction-side surface meshes. From left to right: reference structured mesh, Centaur mesh, Solar mesh.

3.2 Centaur mesh

Centaursoft’s mesh generator accepts IGES geometries, but uniformly discretises the surfaces (by default using 100 points in each direction) prior to mesh generation. For this reason high curvature zones like the wing leading edge have to be separated from the main wing surface to be able to retain the curvature information in the discretised form. Alternatively one can choose to use more discretization points, but this will increase the memory requirements a lot. To give an order of magnitude, the computer on which the meshes have been created has 4GB of RAM, and this value was exceeded when trying to discretise the complete wing surfaces with an acceptable accuracy.

The separation of surfaces in zones (called "groups" in Centaur) and the creation of boundary surfaces are similar to the method explained for Solar. Mesh parameters (sources) can be specified for the geometry (surfaces, curves and points) or arbitrarily in the computational domain using the graphical interface.

No hard-coded limit for the prismatic layer thickness is imposed in Centaur, but the merging between prisms and tetrahedra can fail in regions of high curvature if the prism layer thickness is too high, especially when the cells’ aspect ratio on the surface is large (i.e. at the wing leading edge).

The triangular surface mesh is generated using an advancing front technique; it is possible to generate a structured surface mesh on (almost) rectangular surfaces with relatively low aspect ratio (less than 10). In the present work the slat leading edge has been split to retain the curvature information and is meshed with structured, anisotropic quadrilaterals. The prismatic layer is created using an advancing layer technique, while the tetrahedral part is constructed using an advancing front strategy.

Centaur automatically refines the intersection between 2 surfaces if there is an angle lower than a predefined value (100° by default). As a result the prismatic layer at the wing-fuselage intersection is thinner than for the Solar mesh, but the advantage is a better resolution in the tetrahedral part in this region (Figure 1).

The mesh smoothing is performed directly by Centaur in the mesh generation process, so it is not necessary to use the DLR-TAU tools for this task.

The final Centaur mesh used in the study has roughly 10.8 million points and 40 prismatic layers (Figure 2 centre).

4 CFD RESULTS

4.1 Results at the reference conditions

CFD computations are performed on both unstructured meshes with the 3 selected turbulence models, and compared to the reference results obtained on the structured mesh with Menter’s $k-\omega$ -SST turbulence model.

Table 1 shows the difference, in absolute value, between the aerodynamic coefficients computed on the 2 unstructured meshes and the reference CFD result. Additionally the loads are decomposed in wing and fuselage component. The conditions are the ones

	Solar									Centaur					
	SAE			k ω			RSM			SAE			k ω		
	W	F	T	W	F	T	W	F	T	W	F	T	W	F	T
CL [10 ⁻⁴]	6	2	5	1	4	3	8	15	23	23	4	19	7	8	1
CD [10 ⁻⁴]	4	0	4	2	1	3	4	4	8	1	1	2	1	2	0
CDP [10 ⁻⁴]	3	1	4	3	1	4	4	4	8	1	1	2	1	2	0
CDV [10 ⁻⁴]	1	1	1	1	1	0	0	0	0	1	0	1	1	1	2
CMy [10 ⁻⁴]	21	3	18	10	9	2	23	24	1	32	2	30	16	1	16

Table 1: Absolute value of the difference between unstructured mesh CFD results and the validated CFD result on the structured mesh. $Re = 22.5 \cdot 10^6$, $M = 0.25$, $\alpha = 11.22^\circ$. Column W, F and T refer respectively to the loads on the wing, on the fuselage, and the sum of both components.

	Solar			Centaur	
	SAE	k ω	RSM	SAE	k ω
CL	0.96	0.97	0.80	0.83	1.01
CD	0.71	1.21	1.57	0.86	0.79
CMy	2.00	0.67	1.17	4.00	1.67

Table 2: Difference between unstructured mesh computations and WTT results normalised with the corresponding deviation of the validated structured mesh result. $Re = 22.5 \cdot 10^6$, $M = 0.25$, $\alpha = 11.22^\circ$.

taken as reference: Reynolds number $22.5 \cdot 10^6$, Mach number 0.25 and angle of attack 11.22° . The RSM computation on the Centaur mesh did not converge, so it is not shown here. All turbulence models give satisfying results, with the Spalart-Allmaras model showing higher discrepancy in terms of wing pitching moment. This suggests a difference in pressure distribution, probably due to differences in the main vortex detection. The RSM computation on the Solar mesh also experiences large pitching moment discrepancies both on the wing and the fuselage. Interestingly these effects compensate so that the total value does not differ much from the reference.

For assessing the overall capabilities of the unstructured meshes, the difference between the loads obtained in the CFD and those measured during the wind tunnel tests are shown in Table 2. In this table values are expressed relative to the difference between WTT and validated CFD, in such a way that a value of 1 expresses a similar accuracy to the structured mesh results.

From a purely qualitative point of view, the flow physics is correctly captured using the unstructured meshes, as can be seen in Figure 3 and 4. Figure 4 in particular uses the normalised helicity value as a vortex detector. This value is computed as follows:

$$H_n = \frac{\vec{u} \cdot \vec{\omega}}{|\vec{u}| \cdot |\vec{\omega}|} \quad (1)$$

where \vec{u} is the velocity vector and $\vec{\omega}$ the vorticity vector. In fact the normalised helicity represents the cosine of the angle between helicity and vorticity and thus is a good detector of vortical flow: in the vortex core the vorticity vector is aligned with the velocity vector,

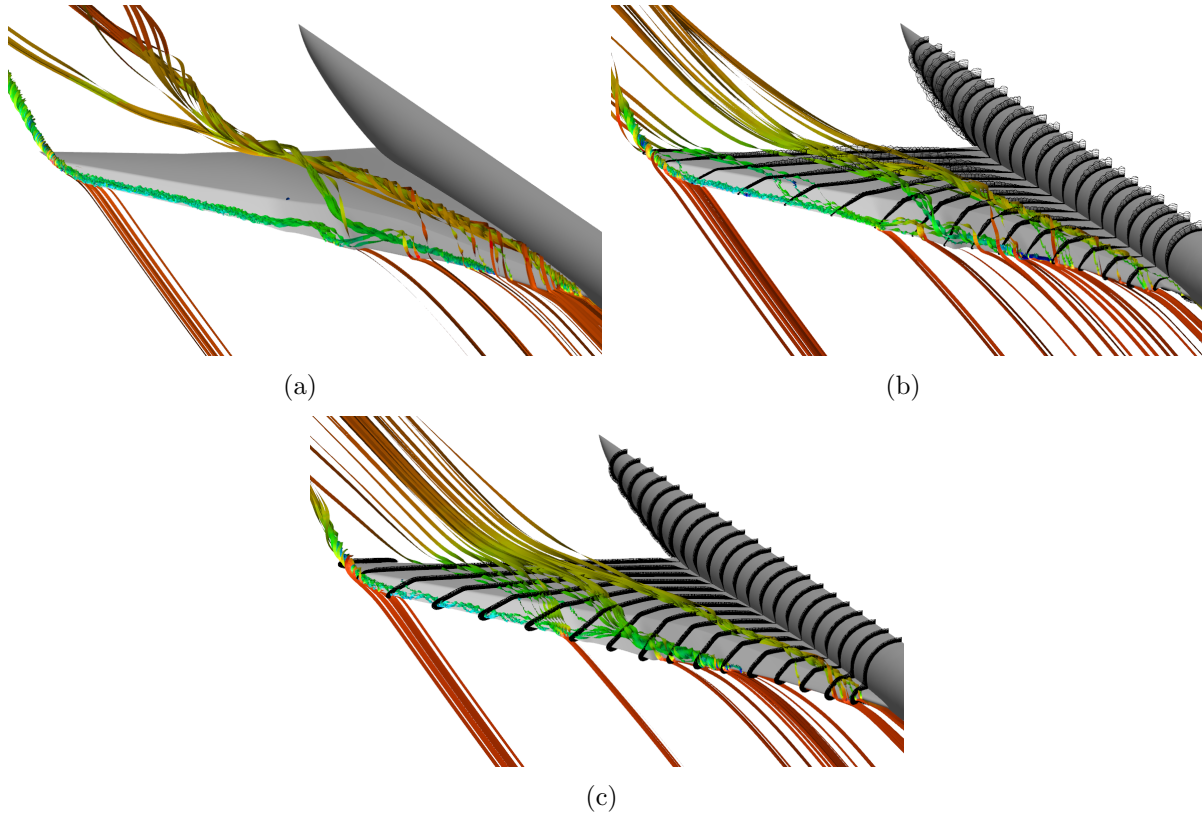


Figure 3: Streamlines illustrating the vortical flow on (a) the structured mesh, (b) the Solar mesh, (c) the Centaur mesh. Some prismatic layer mesh cuts are shown for the unstructured meshes. $Re = 22.5 \cdot 10^6$, $M = 0.25$, $\alpha = 11.22^\circ$.

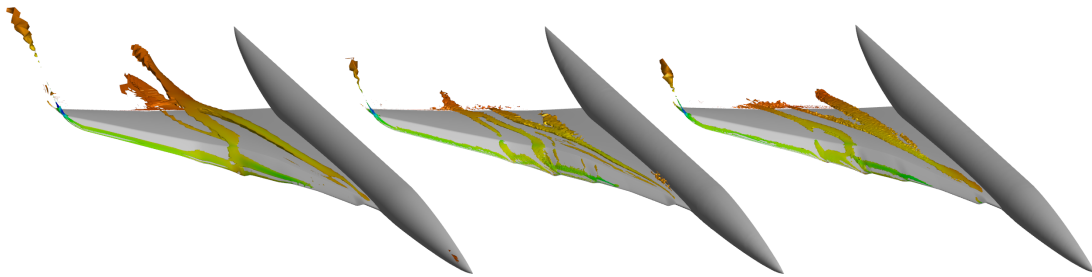


Figure 4: Vortical flow topology highlighted by normalised helicity isosurfaces of $|H_n| = 0.95$ painted according to the pressure value. $Re = 22.5 \cdot 10^6$, $M = 0.25$, $\alpha = 11.22^\circ$. $k-\omega$ -SST turbulence model. From left to right: structured mesh, Solar mesh, Centaur mesh.

resulting in a H_n value of ± 1 , with the sign depending on the rotation direction.

The main vortex, developing at the wing root, and the vortices on the inboard and outboard slats are all detected. The main vortex, however, seems to be confined in the prismatic layer, and looks more flattened than on the reference result. This behaviour is caused by the dissipative effect of the tetrahedral mesh. Moreover the unstructured

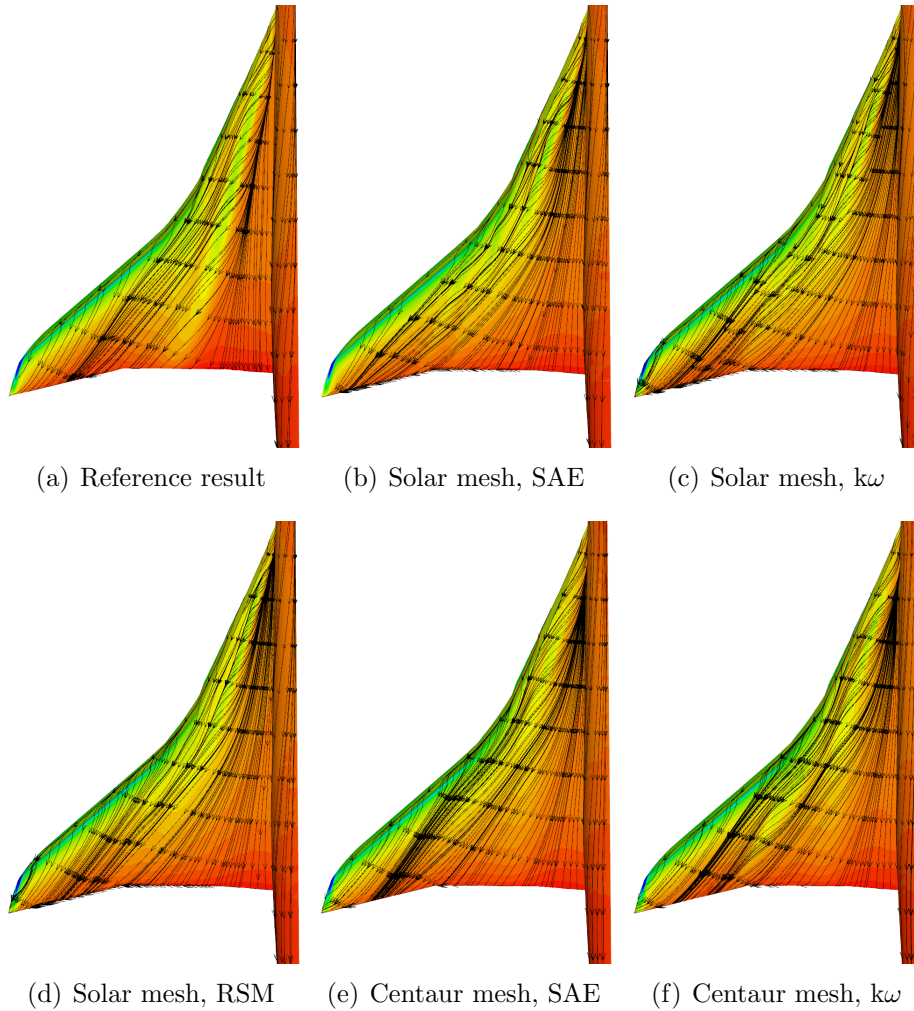


Figure 5: Skin friction plots on the suction side of the wing, colours show the pressure coefficient. $Re = 22.5 \cdot 10^6$, $M = 0.25$, $\alpha = 11.22^\circ$.

meshes cannot track the main vortex in the wake region. The Solar mesh has even trouble in keeping track of the vortex in the wing trailing edge region (Figure 4).

Additionally, the unstructured meshes predict a vortical structure developing from the inner end of the outboard slat. This is not seen in the structured mesh. It is difficult to say if this flow feature is incorrectly predicted by the unstructured meshes, or simply not captured by the structured mesh, which is much coarser than the unstructured ones in the spanwise direction.

In Figure 5, which shows the skin friction lines, it can be seen that the location of the main vortex in all the unstructured mesh simulations seems to differ from the reference result. The computation on the Centaur mesh with the $k-\omega$ turbulence model seems to give the better prediction in terms of vortex location.

The vortex is stronger in the Solar mesh result with SA model (Figure 6, cut plane 1)

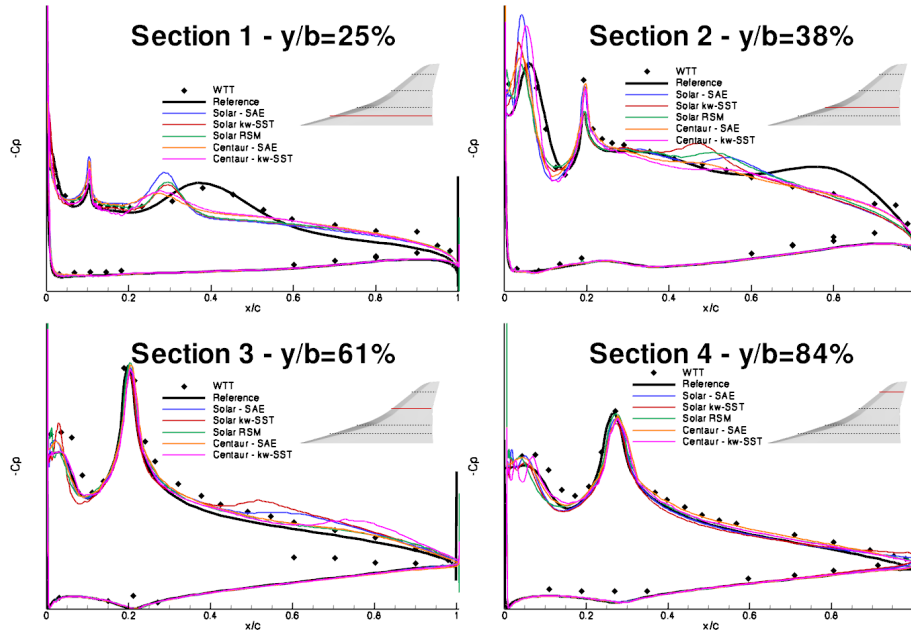


Figure 6: Pressure coefficient distribution on selected iso- y wing sections. $Re = 22.5 \cdot 10^6$, $M = 0.25$, $\alpha = 11.22^\circ$.

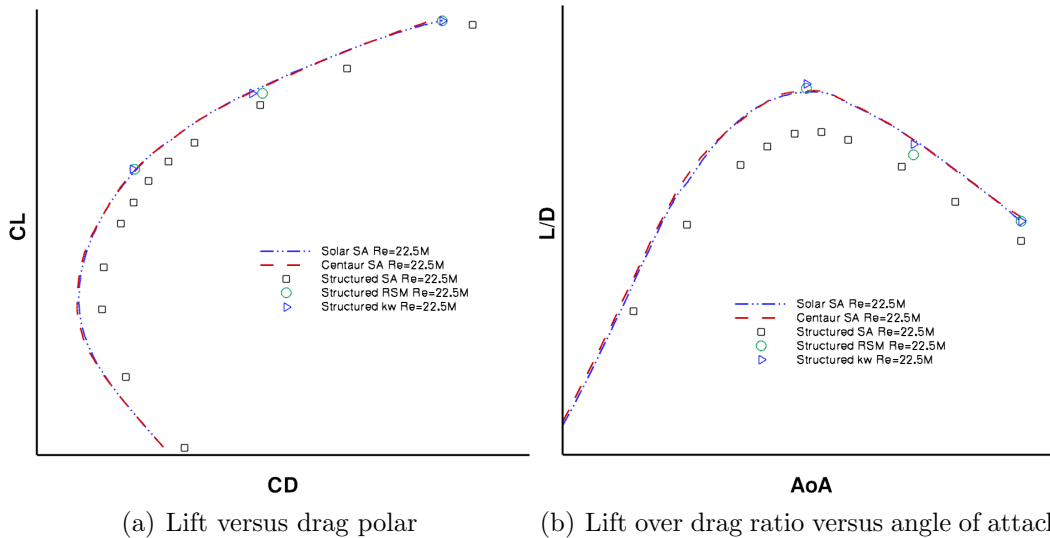
compared to the reference results. The Solar mesh coupled with the $k-\omega$ and RSM models give the right vortex intensity, as far as the pressure level on the wing goes. Results on the Centaur mesh show a weaker vortex which is dissipated too quickly (it is almost not detected on Figure 6, cut plane 2). Solar results still show the vortex on section 2, albeit too upstream compared to the reference (for which the vortex crosses section 2 near the trailing edge).

Suction peaks at the drop-nose slat's deflection line are overestimated (compared to the reference result), especially when using the Spalart-Allmaras turbulence model, and are in best agreement with the reference results in the case of the Solar mesh with the $k-\omega$ and RSM turbulence models. Discrepancies near the slat leading edge between results on structured and unstructured mesh could be due to the fact that the unstructured meshes are more refined in that region and can capture smaller flow details. Unfortunately pressure data coming from wind tunnel do not have the required resolution to crosscheck this result.

On the wing pressure side, where the flow is attached, all meshes and all turbulence models are able to get the right pressure distributions. The discrepancies between CFD and WTT on the pressure side (see for instance section 3 in Figure 6) are due to the 3 struts mounting system that locally modifies the flow.

4.2 Complete polar

A complete polar has been computed on both unstructured meshes at the reference flow conditions using the Spalart-Allmaras turbulence model.

Figure 7: Complete polars at $Re = 22.5 \cdot 10^6$.

From the graphs in Figure 7 it can be seen that results on the 2 unstructured meshes are very similar. The results are compared to some results on the structured mesh: 3 angles of attack (11.22° , 9.22° , 7.22°) for the $k-\omega$ -SST and RSM turbulence models and a complete polar for the Spalart-Allmaras turbulence model.

The results on the unstructured meshes match with remarkable accuracy those on the structured mesh with $k-\omega$ or RSM turbulence models. On the contrary the (non-validated) results on the structured mesh using the SA turbulence model drastically overestimate the drag. This discrepancy of the SA model when coupled with the structured mesh is unclear: on the unstructured meshes the SA and $k-\omega$ results are of similar quality.

Based on these results, successive in depth studies will be performed on Solar meshes, due to their easier setup process, especially with respect to CAD preparation. The Spalart-Allmaras turbulence model is chosen as the preferred turbulence model for the remainder of this work thanks to its robustness and convergence speed. Additionally the load prediction capabilities achieved with this model are satisfying.

4.3 Reynolds effect analysis

For studying the reliability of the CFD method developed, some computations at lower Reynolds numbers have been performed. A new Solar mesh has been created using the same input sources and setup as for the mesh at flight Reynolds number, but increasing the first cell height in order to obtain an appropriate y^+ at $Re = 6.5 \cdot 10^6$. This mesh is also used for the computations at $Re = 5 \cdot 10^6$, since the required y^+ does not change too much between the two Reynolds numbers.

In order to be consistent with the wind-tunnel tests at lower Reynolds number, the Mach number was lowered accordingly. The Mach number is thus changed to $M=0.232$

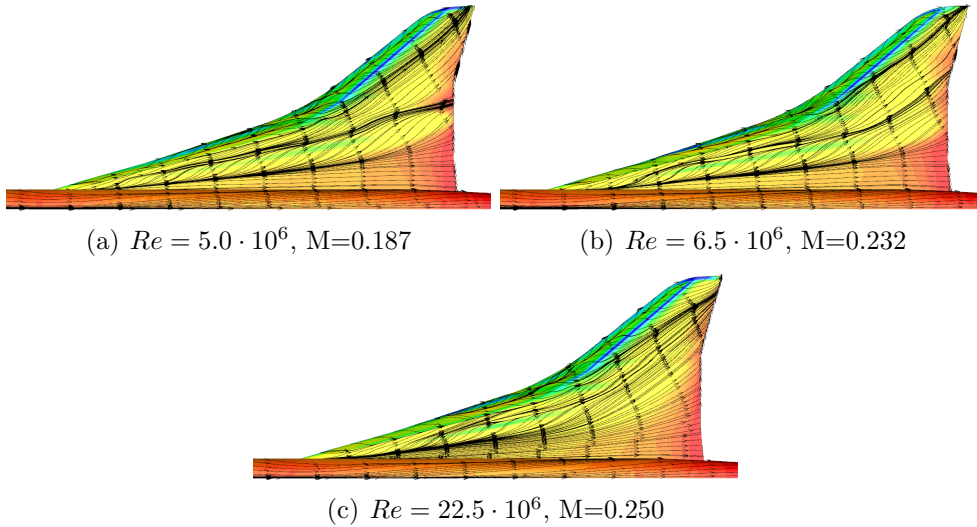


Figure 8: Skin friction plots on the suction side of the wing for 3 Reynolds numbers, colours show the pressure coefficient. Solar mesh, $\alpha=11.22^\circ$.

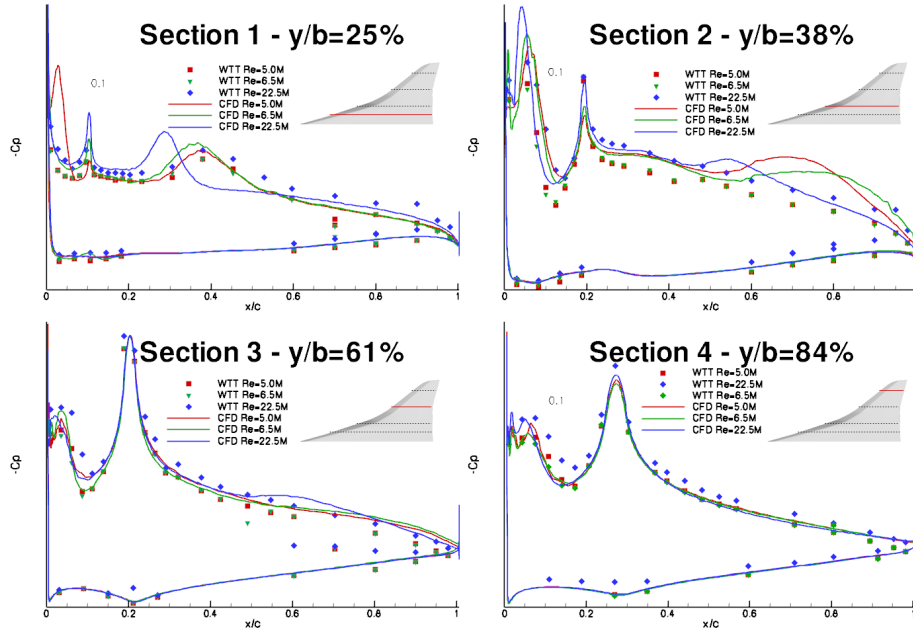


Figure 9: CFD and WTT comparison of pressure coefficient distributions on selected iso-y wing sections for three different Reynolds numbers at $\alpha=11.22^\circ$.

for the $Re=6.5 \cdot 10^6$ case and to $M=0.187$ for the $Re=5 \cdot 10^6$ case. Since the compressibility effects are very low at such velocity, the Mach number change shouldn't affect the flow physics.

Figure 8 shows the skin friction lines at $\alpha=11.22^\circ$ for the 3 Reynolds numbers considered. From the image it is clear that at low Reynolds the main wing vortex is better

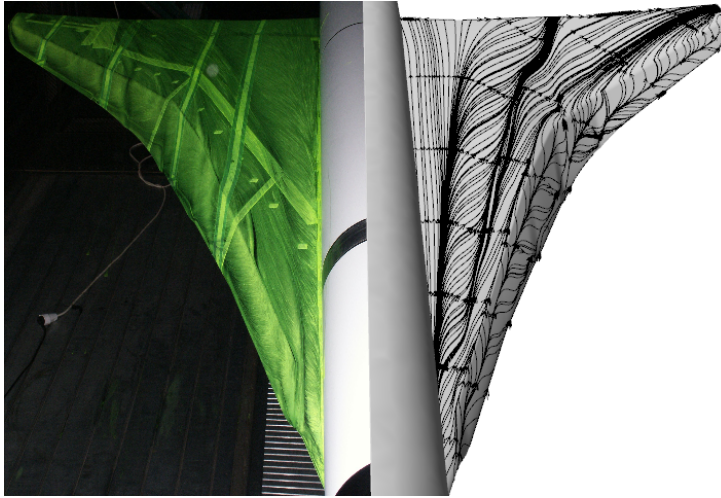


Figure 10: WTT and CFD comparison of skin friction lines for the case $Re=5 \cdot 10^6$, $M=0.187$, $\alpha=11.22^\circ$.

captured. This is due to the increased thickness of the prismatic layer, made possible by a larger first cell height. The improvement can also be observed in the first section of Figure 9: the vortex location is well predicted and the suction effect only slightly overestimated.

While in the high Reynolds case the CFD predicts that the main vortex crosses section 2 more upstream than in the experiments, at low Reynolds the opposite happens: in the wind tunnel tests the main vortex exhibits more cross-flow than in the simulation, thus crossing section 2 sooner. A comparison between an oil flow image and a plot of skin friction lines based on the CFD result is made in Figure 10. The discrepancy in the vortex direction can be clearly seen; nonetheless the overall agreement in the flow physics is remarkable.

A complete polar has also been computed at these 2 Reynolds numbers. Figure 11(a) shows the lift versus drag polar for all 3 Reynolds numbers studied. These polars are compared to validated CFD results on the structured mesh and to wind tunnel data for the low Reynolds number cases. We can see that for the reference conditions considered (that is, at $\alpha=11.22^\circ$), which correspond to the right end of the CFD curves, the agreement with the wind tunnel tests is good. In the maximum lift-over-drag ratio region, however, the drag value is underestimated at low Reynolds; this translates to an overestimation of the maximum L/D. The discrepancy could be explained by the fact that the 1:22 wind tunnel model was developed primarily for use in the ONERA-F1 wind tunnel, which is larger than the DNW-NWB tunnel. As a result in the DNW-NWB facility the effect of the wind tunnel walls could have had an impact on the results for some angles of attack.

Structured and unstructured results are very similar, showing that the unstructured meshes can reach similar accuracy as the state of the art approach.

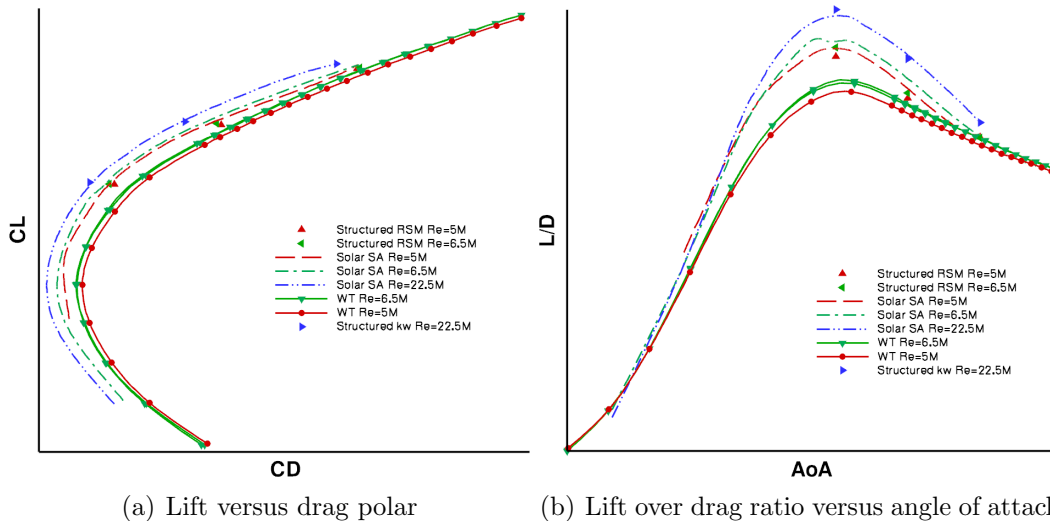


Figure 11: CFD polars at 3 Reynolds numbers compared to WTT (for low Reynolds) and to structured mesh results.

5 DISCUSSION

Results outlined in the previous section show that unstructured meshes are suitable for the computation of vortex dominated flows. In terms of forces and moments, the two hybrid meshes tested give results in line with the validated CFD results on the structured mesh. In comparison to the low Reynolds wind tunnel data, however, the drag is underestimated in all CFD results.

The unstructured meshes are able to capture the main flow features thanks to the good quality of the prismatic layer. Without grid adaptation however, the vortices tend to quickly dissipate in the tetrahedral region. This is the reason why the prism layer has to be maximized. The good capturing of the main vortex in the low Reynolds cases, where the prismatic layer is thicker, is a proof of this fact.

The vortices quickly dissipate downstream of the wing, as it is seen in Figure 3 and 4. This cannot be avoided without using grid adaptation or an extremely fine mesh. Nevertheless the effect on loads and in particular on drag seems to be low.

Two opposite trends appear in regard to turbulence modelling: when using the structured mesh the Spalart-Allmaras model is too dissipative and predicts higher drags than the 2 other models considered. On the unstructured meshes however SA gives as good results as the more complex models, especially for the lift and the drag coefficients, only a relatively small discrepancy for the pitching moment value is observed. All in all, since the computations with the SA turbulence model were obtained with the best convergence rate without stability issue, this model is selected to be used in optimization context.

In fact when using the $k-\omega$ -SST model the simulation is not completely stable and it is sometimes necessary to start with a simpler and more stable $k-\omega$ model (Wilcox model was chosen for this) and/or start with an upwind space scheme. The RSM computation

was started from a converged $k\text{-}\omega$ -SST solution, by setting the turbulence variables in the field to their free-stream values. This means that $k\text{-}\omega$ and RSM computations are more time consuming not only because more equations have to be solved (7 and 12 for $k\text{-}\omega$ and RSM respectively, compared to 6 for Spalart-Allmaras) but also because they require some initialization steps and more iterations to converge.

The selection of the hybrid mesh generators is more difficult. Both mesh generators tested give similar results, so it is difficult to make a choice based solely on the accuracy of the predicted loads. When considering the mesh generation process, however, some differences are found. Firstly, Centaur requires more CAD preparation in order to correctly mesh the geometry: the wing leading edge has to be reworked to get panels that can be meshed using structured quadrilaterals, and to be able to get the right leading edge curvature in the discretised geometry used for the surface mesh generation. Secondly, the time required for the complete mesh generation is higher for Centaur (depends on the settings chosen, but was around 4 hours for this configuration) than for Solar (about 1 hour plus the mesh modification and the smoothing, in total around 1 and a half hours). On the other hand Centaur was found more stable than Solar: Solar tends to exit with an error when merging far-field mesh and prism layer if the anisotropy of the surface quadrilaterals is set too high. Decreasing the anisotropy (thus increasing the mesh size) solves this problem. Finally, it was previously observed during the fourth AIAA CFD Drag Prediction Workshop that the Solar mesh generator is able to generate family of meshes with constant high quality [14] which is a key element in optimization context.

Based on these considerations, the next optimization chain will include the automatic mesh generation tool Solar with the CFD computations done using the Spalart-Allmaras turbulence model.

6 CONCLUSIONS

In this paper it has been shown that unstructured, hybrid meshes are suited for the simulation of complex flow fields like the airflow past a highly swept delta wing at high angle of attack. Even without relying on grid adaptation, like commonly done when using this approach, the main flow features are accurately predicted on meshes containing about 10 million points. However, a thick prismatic layer is capital for the correct prediction of the vortex strength and position. Finally, aerodynamic loads can be predicted with similar accuracy as with the structured mesh.

For building the aerodynamic optimization chain, the Solar mesh generator is found to be the best candidate and the Spalart-Allmaras is considered as the most suited turbulence model for solving the Navier-Stokes equations in a stable and efficient way.

REFERENCES

- [1] U. Herrmann, A. Press, C. Newbold, P. Kaurinkoski, C. Artiles, J.V. Muijden, and G. Carrier, Validation of European CFD Codes for SCT low-speed high-lift Computations, In proceedings of the *19th AIAA Applied Aerodynamics Conference*, Anaheim, USA (2001).
- [2] J. van Muijden and B. Elsenaar. Numerical prediction capabilities and analysis of flow development for a supersonic civil transport at low speed, In proceedings of the *CEAS Aerospace Aerodynamics Conference*, Cambridge, UK (2002).
- [3] M. Widhalm, A. Schütte, T. Alrutz and M. Orlt, Improvement of the Automatic Grid Adaptation for Vortex Dominated Flows using Advanced Vortex Indicators with the DLR-TAU Code, Notes on Numerical Fluid Mechanics and Multidisciplinary Design, *Springer Vol. 96* (2006).
- [4] J. Brezillon, R.P. Dwight and J. Wild, Numerical Aerodynamic Optimisation of 3D High-Lift Configurations, *26th Congress Of The International Council Of The Aeronautical Sciences*, Anchorage, USA (2008).
- [5] U. Herrmann, Low-Speed High-Lift Performance Improvements obtained and validated by the EC-project EPISTLE, In proceedings of the *24th ICAS Conference*, Yokohama, Japan (2004).
- [6] U. Herrmann, Analysis of numerical prediction capabilities for SCT low-speed high-lift flows, EPISTLE internal report (2001).
- [7] CentaurSoft, <http://www.centaursoft.com>
- [8] D. G. Martineau, S. Stokes, S. J. Munday, A. P. Jackson and B. J. Gribben, Anisotropic Hybrid Mesh Generation for Industrial RANS Applications, AIAA-paper 2006-534, *AIAA Aerospace Conference*, Reno, USA (2006).
- [9] D. Schwamborn, T. Gerhold and R. Heinrich, The DLR TAU-Code: Recent Applications in Research and Industry, *ECCOMAS CFD 2006*, Egmond aan Zee, Netherland (2006).
- [10] P.R. Spalart and S.R. Allamaras, A One-Equation Turbulence Model for Aerodynamic Flows, AIAA Paper 92-0439 (1992).
- [11] J. Edwards and S. Chandra, Comparison of Eddy Viscosity-Transport Turbulence Models for Three-Dimensional Shock-Separated Flowfields, *AIAA Journal of Aircrafts*, **Vol. 34**, No. 4, pp. 756-763 (1996).
- [12] F.R. Menter, Two-Equation Eddy Viscosity Turbulence Models for Engineering Applications, *AIAA Journal*, **Vol. 32**, pp. 1598-1605 (1998).

- [13] B. Eisfeld and O. Brodersen, Advanced Turbulence Modelling and Stress Analysis for the DLR-F6 Configuration, AIAA-Paper 2005-7727 (2005).
- [14] O. Brodersen, S. Crippa, B. Eisfeld, S. Keye and S. Geisbauer, DLR Results from the Fourth AIAA CFD Drag Prediction Workshop. *AIAA Applied Aerodynamics Conference*, Chicago, USA (2010).